Large Gain Amplification Mechanism for Piezoelectric Actuators Utilizing a Rolling Contact Joint

by

James Torres

B.S., Mechanical Engineering, Massachusetts Institute of Technology, 2010

Submitted to the Department of Mechanical Engineering in partial fulfillment of the requirements for the degree of

Master of Science in Mechanical Engineering

at the

MASSACHUSETTS INSTITUTE OF TECHNOLOGY

June 2012

Author .....
Department of Mechanical Engineering
June 1, 2012

Certified by .....
H. Harry Asada
Ford Professor of Mechanical Engineering
Thesis Supervisor

Accepted by .....
David E. Hardt
Chairman, Department Committee on Graduate Students
Department of Mechanical Engineering

Design and Analysis of a Displacement Amplification Mechanism for Piezoelectric Actuators

by

James Torres

Submitted to the Department of Mechanical Engineering
on June 1, 2012, in partial fulfillment of the
requirements for the degree of
Master of Science in Mechanical Engineering

Abstract

Due to the limited displacement of piezoelectric stack actuators, common practice is to use some form of displacement amplification mechanism. An efficient, heavy-duty displacement amplification mechanism for piezoelectric stack actuators is presented in this thesis. The displacement amplification gain is increased by a factor of more than 100 in a single stage by using a buckling mechanism combined with a novel rolling contact design. Unlike traditional flexure-type monolithic mechanisms, which are accurate but inefficient and fragile, the new mechanism consists of all rolling contact couples, providing high stiffness, durability and energy efficient characteristics. Furthermore, a new design of preloading mechanism using shape memory alloy doubles the possible cyclic work output and provides a desirable restoring force for constraining the rolling contact mechanism stably and efficiently. This mechanism is intended to be interfaced with a sinusoidal gear cam that acts as the load. The dynamics of the system are derived and are shown to be fifth order. Due to the significantly nonlinear amplification caused by the buckling phenomenon and the gear, the dynamics are run in simulation to gain insight into the dynamic performance of the actuator. There is shown to be an optimal speed at which to run the actuator to maximize the possible power output. Furthermore, due to the simple binary control significant benefits are achieved by varying the control timing based on the velocity to ensure the force and velocity of the output are in phase. Finally, a prototype was constructed to compare to the static model. The prototype had a peak to peak displacement of 6.8 mm, an amplification of over 150, and produced a peak charged force of 56 Newtons.

Thesis Supervisor: H. Harry Asada
Title: Ford Professor of Mechanical Engineering

Acknowledgments

First and foremost, I would like to thank Professor Asada. Over the past two years he has acted as my mentor and has helped develop my creativity, an attribute I never considered a strength prior to working with him. I greatly appreciate the patience he afforded me, while constantly pushing to me strive forward.

Furthermore, I would also like to thank the Sumitomo Heavy Industries, for their generous financial support that allowed me to pursue this captivating research and continue to grow as a student, an engineer, and a person.

I am grateful to my colleagues at the d'Arbeloff Laboratory. They were always available to provide another mind to brainstorm with, or a laugh when needed. Specifically, I thank Shinichiro Tsukahara who unquestionably helped me develop as an engineer, who taught me practices and tips not available in the classroom and how to attack a problem from all directions, and who I am blessed to call a friend.

Finally, and most importantly, I must thank my parents for their unwavering love and who serve as constant pillars of support. I am proud to say that I would not be the person I am today without the teaching, motivation, and care they have always provided me.

Contents

List of Figures

List of Tables

Chapter 1

Introduction

At the forefront of linear actuator research is the desire to develop an actuator that is competitive across several design parameters, including weight, efficiency, bandwidth, force, and stroke. Piezoelectric actuators, in particular PZT stack actuators, compare favorably to other smart material actuators, such as shape memory alloy and hydraulic actuators, in most of these parameters, with the only significant exception being stroke. Their insufficient strain, typically around 0.1%, limits their typical applications to high precision nano- and micro- scale mechanisms. [1] Therefore, over the past few decades, researchers have striven to develop amplification mechanisms that provide a larger stroke while maintaining many of the desirable characteristics of the other design parameters.

Displacement amplification mechanisms typically fall into one of three categories. The first group is internally leveraged mechanisms, which include cantilevered designs and predominantly rely on the d_{31} mode of actuation as opposed to the d_{33} mode in stack actuators. These mechanisms do not significantly sacrifice weight or efficiency, but greatly reduce the potential output force. These particular mechanisms are best suited for microelectronic mechanical systems (MEMS) [2] and audio applications [3] due to their small displacements and forces and high bandwidth. [4]

The next group is frequency leveraged mechanisms. These mechanisms utilize piezoelectric stacks' high bandwidth in an inch worm type setup to provide continuous motion. This design requires extensive use of friction to bear the output load which

can limit efficiency and the stall load. These actuators excel in high precision, low load applications such as fiber optic and wire electrical discharge machining positioning. [4]

The final group is externally leveraged mechanisms. These mechanisms can be significantly larger in size and weight and therefore sacrifice bandwidth as well as power density. Their mechanical complexity ranges from simple lever arms to more elaborate flextensional devices. The flextensional devices almost exclusively use flexures for their repeatability and ease of manufacturing. The flexures are arranged in a shallow angle compared to the axis of the PZT stack where the produces amplifications around one order of magnitude. [5][6][7] These amplifications can be increased further by nesting one set of flexures within another. [8][9][10] Typically, these actuators have a significant drop in efficiency at each layer due to the energy loss associated with the compliance of the mechanism. There are several other designs including the "V-Stack," [11] the "double X-frame," [12] and a unit for helicopter flap control [13] that use multiple PZT stacks to reduce the number and size of the flexures and subsequently increase the output force and efficiency. [4]

This paper focuses on the dynamic performance of a specific externally leveraged mechanism. The fundamental concept of the design discussed in this thesis relies on the large amplification ratios associated with the non-linear phenomenon of buckling. [14][15] Consider two identical piezoelectric stack actuators constrained collinearly in between two rigid walls. At each interface there is an ideal rotational joint, in this case ideal is defined as infinitely rigid with no friction. As the piezoelectric stacks are energized, they will tend to rotate and the center joint, referred from here on as the keystone, will displace orthogonally to the axis of the PZT stacks. The keystone displacement can typically be over 100 times the displacement of the piezoelectric stack in a single stage.

Chapter 2

Mechanism Design Concepts

2.1 Constant Preload

A preload is common in mechanical systems to reduce slop, increase stiffness, and maintain contact between surfaces. This section will describe the need for and benefits of such a preload along with how to implement it. The amount of work that a PZT actuator can produce in one cycle of operation is obtained as the area contained within a closed loop trajectory in the force-displacement plane. There are two boundary conditions that constrain the stack actuator subsequently limit the cyclic work output. First, the stack has an acceptable voltage band; and second, it cannot be placed in tension. Both of these constraints are to prevent permanent damage to the stack actuators. The effect of these two constraints on output are obvious when considering the trajectory in Fig. 2-1. The voltage and force constraint are illustrated by the trajectory from point 2 $\rightarrow$ 3 and 3 $\rightarrow$ 1, respectively. In order to maximize the cyclic work output, one imposed constraint is added: while charging there is no displacement. The maximum cyclic work output, W_{lone}, is then defined in 2.1, z_f is the PZT stack free displacement, F_B is the blocking force, and F_{PZT} is the output force.

$$W_{lone} = \oint_{1\to 2\to 3} F_{PZT} \cdot dz = \frac{F_B z_f}{2} \tag{2.1}$$

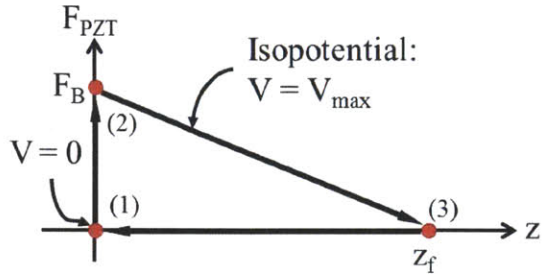

Figure 2-1: An idealized trajectory for a single PZT stack actuator with a physical constraint on voltage and output force and an imposed constraint on displacement, where F_B is the blocking force, z_f is the free displacement and V is the applied voltage.

The cyclic work output extracted can be increased further by utilizing two methods, adding one more mechanical constraint which limits the displacement during charging and discharging; and adding a constant preload force to the PZT stack between two caps, as shown in the trajectory $1 \to 2 \to 3 \to 4$ in Fig. 2-2. In the figure the z_o and $F_{PZT,o}$ axes are the initial axes associated with Fig. 2-1 and the z and F_{PZT} axes are with reference to the caps used to preload the PZT stack. The increase in the cyclic work output is due to the fact that the preloaded PZT stack-cap assembly can be placed in tension, whereas the lone PZT stack cannot. The increased preloaded cyclic work output, $W_{preload}$, is defined in Eq. 2.2.

$$W_{preload} = \oint_{1\to 2\to 3\to 4} F_{PZT} \cdot dz = F_B z_f = 2W_{lone} \tag{2.2}$$

The two mechanical constraints added, however, have a finite non-zero stiffness associated with them. A compliance in the mechanism that prevents the displacement during charging and discharging creates the sloped trajectories $1 \to 2'$ and $3' \to 4'$, whereas a stiffness in the preload mechanism creates the steeper trajectories $2' \to 3'$

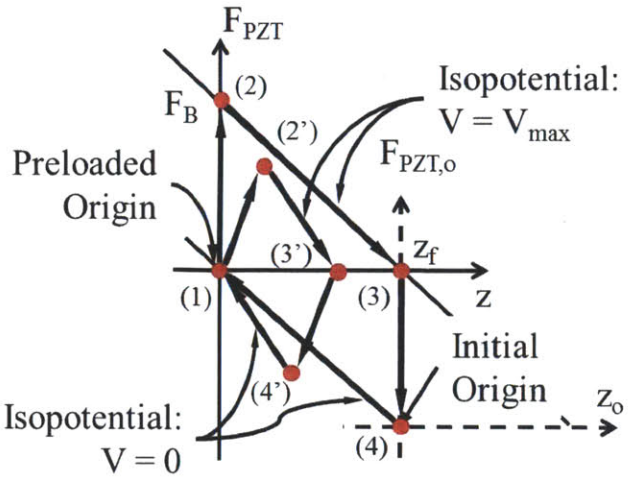

Figure 2-2: An idealized trajectory for a preloaded PZT stack actuator assembly.

and $4' \rightarrow 1$. Even if these mechanisms modeled as lossless, the cyclic work output can be reduced substantially.

2.2 Buckling Amplification

In order to overcome the PZT actuator's limited strain, an amplification mechanism that relies on controlled structural buckling is utilized for its high amplification ratio. Figure 2-3 shows the schematic of the buckling displacement amplification mechanism. Two PZT stack actuators are linearly aligned with a connecting component between them, referred to in this paper as the "keystone," that displaces perpendicular to the original axis of alignment, as shown in the figure. As the PZT stacks elongate, they rotate causing a phenomenon similar to buckling. This "buckling" displacement amplification can increase displacement by a factor of 100 or greater in a single stage: an order of magnitude higher amplification gain compared to rhombus-type mechanisms [16] and others. The buckling mechanism allows for bi-polar swing of the output displacement across a kinematic singular point in the middle. This kinematic singularity will be addressed later in the design.

The buckling amplification units allow for mechanical work to be more easily extracted from the PZT stacks, but are not conducive to direct application to a

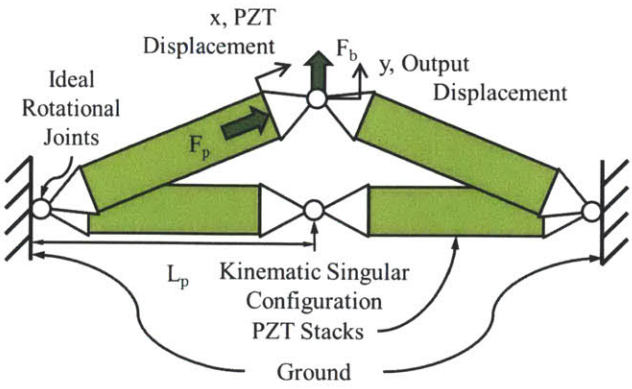

Figure 2-3: A basic schematic of the buckling amplification mechanism.

load. As shown in Fig. 2-4, the force-displacement relationship is highly non-linear. Furthermore, the fact that PZT stacks are a capacitive electrical loads with high bandwidth prevents useful strategies, such as pulse width modulation, from being effective to modulate the applied voltage.

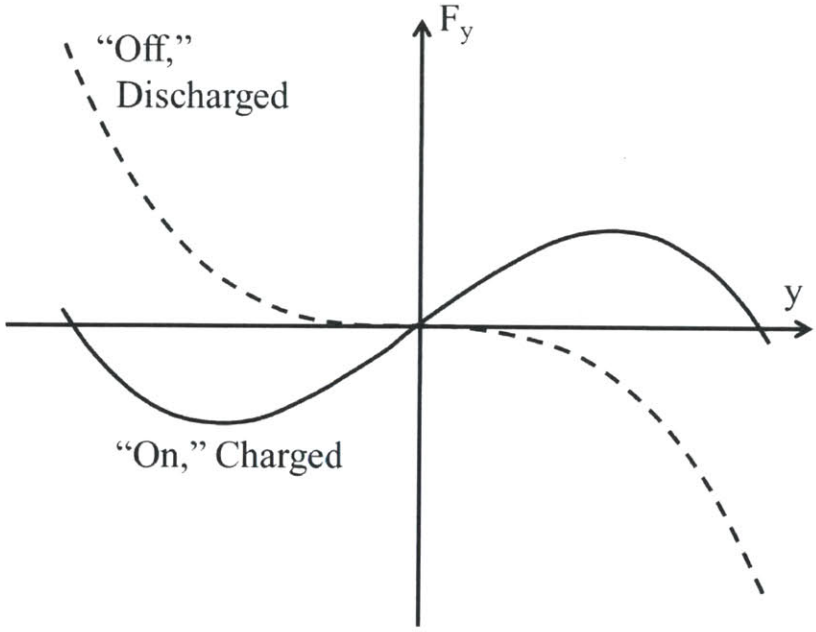

Figure 2-4: A general force-displacement trajectory for the activated and deactivated buckling mechanism.

While the buckling amplification concept has unique features, its proper implementation is a challenging task. The existing implementation is based on flexure design. Although flexure mechanisms are simple to fabricate and accurate, the per-

formance of the existing flexure-type designs are limited due to friction and parasitic compliance within the structure, predominantly at the rotating joint, which reduces the amount of work being transmitted to the output. By replacing flexures with rolling contact joints, however, a significant portion of the unwanted elastic resistance can be removed by increasing the structural rigidity and subsequently leading to a higher efficiency.

The following design requirements for the rotational joint are defined, demonstrating the benefit of the rolling contact joint:

- Amplification: mechanically amplify the piezoelectric stack displacement two orders of magnitude
- Energy efficiency: The mechanical energy transfer loss due to serial compliance and friction should be minimized
- Preload: The system will provide a preload to the PZT stack with a comparatively low stiffness to increase the mechanical work output per cycle

2.2.1 Rolling Contact Joint

Fig. 2-5 shows the basic schematic of a flexure-free, rolling-contact buckling mechanism for PZT displacement amplification. It consists of three major components, aside from the PZTs themselves:

- Caps: workpieces placed at both ends of each PZT stacks encompassing the PZT stack
- Keystone: a workpiece placed in the middle that serves as an output node connected directly to the load
- Ground: an infinitely rigid structure

The joint is formed by the contacts maintaining a rolling contact. This buckling mechanism contains four rolling contacts where the caps interact with the ground and

keystone. Not shown in the figure, the keystone is constrained to prevent rotation in all 3 axes and translation in X and Z, therefore allowing a single degree of freedom, displacement in Y. As the PZT stacks are activated, they tend to elongate. As a result, the keystone displaces upwards (or downward), and the caps roll without slipping along the ground/keystone.

This mechanism is symmetric with respect to the centerline upon which the keystone moves. The profiles of each pair of caps on each PZT stack are symmetric, and each has the same curvature. Furthermore, the curvature of the ground profile is the same as that of the keystone.

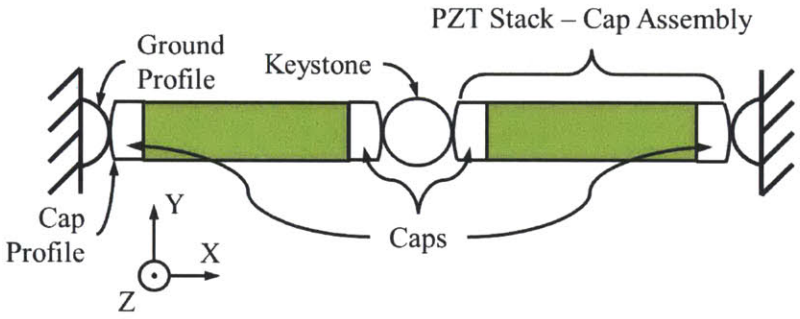

Figure 2-5: A schematic of the rolling contact buckling mechanism.

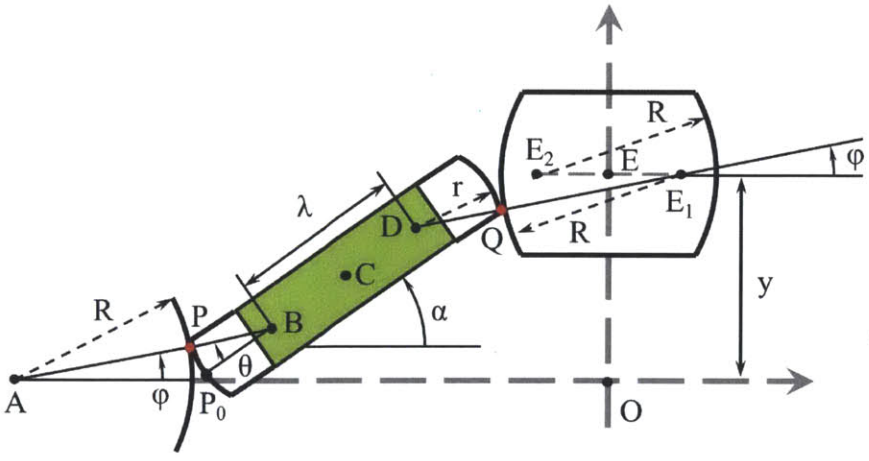

Figure 2-6: A generalized geometry of the rolling contact joint.

Let R be the radius of the ground surface as well as the keystone surface, and r be that of the cap, as shown in Fig. 2-6. Assuming no slip, we obtain

$$R\varphi = r\theta \therefore \theta = \frac{R}{r}\varphi \tag{2.3}$$

where $\varphi = \angle OAP$ is the ground contact angle, and $\theta = \angle PBP_0$ is the cap contact angle shown in the figure. The tilting angle of the PZT stack-cap assembly, α, is given by

$$\alpha = \varphi + \theta, \therefore \alpha = \left(1 + \frac{R}{r}\right)\varphi \tag{2.4}$$

Let λ_0 be the distance between points B and D at rest. At this rest configuration both PZT stacks, caps, and the keystone are aligned, and the PZT stacks are not activated. As both PZT stacks elongate, the distance between B and D becomes $\lambda = \lambda_0 + \Delta\lambda$. Assuming no slip at the rolling contact points we can obtain the displacement of the keystone in the vertical direction. From Fig. 2-6,

$$\begin{aligned} y &= 2\,(R + r)\sin\varphi + (\lambda_0 + \Delta\lambda)\sin\alpha \\ &= 2R\,(1 + \Gamma)\sin\varphi + (\lambda_0 + \Delta\lambda)\sin\{\varphi \cdot (1 + \Gamma)\} \end{aligned} \tag{2.5}$$

where

$$\Gamma = \frac{R}{r} \tag{2.6}$$

Note that, since the keystone is constrained to not rotate, completely symmetric displacements occur at both rolling contact points, P and Q. Since the distance between points A and O is constrained by the ground structure, the distance from the ground to the keystone along the X axis must remain constant:

$$2(R+r)\cos\varphi + (\lambda_0 + \Delta\lambda)\cos\alpha = 2(R+r) + \lambda_0 \tag{2.7}$$

Approximating the cosine function to $\cos\varphi \cong 1 - \frac{1}{2}\varphi^2$, we can solve 2.7 for φ

$$\varphi \cong \sqrt{\frac{\Delta\bar{\lambda}}{(1+\Gamma)\left\{1 + \frac{1}{2}\left(\Delta\bar{\lambda} + \bar{\lambda}_0\right)(1+\Gamma)\right\}}} \tag{2.8}$$

where $\Delta\bar{\lambda} = \Delta\lambda/r$, $\bar{\lambda}_0 = \lambda_0/r$. Substituting this into 2.5 yields the displacement amplification gain:

$$\frac{y_{max}}{\Delta\lambda} \cong 2\sqrt{\frac{(1+\Gamma)\left\{1 + \frac{1}{2}\left(\Delta\bar{\lambda} + \bar{\lambda}_0\right)\right\}}{\left\{1 + \frac{1}{2}\left(\Delta\bar{\lambda} + \bar{\lambda}_0\right)(1+\Gamma)\right\}\Delta\bar{\lambda}}} \tag{2.9}$$

In the case $\bar{\lambda}_0 = 0$, a situation explained next, the amplification gain can be simplified to

$$G = \frac{\Delta y}{\Delta\lambda} = \frac{2y_{max}}{\Delta\lambda} \cong 4\sqrt{\frac{1+\Gamma}{\Delta\bar{\lambda}}} = 4\sqrt{\frac{R+r}{\Delta\lambda}} \tag{2.10}$$

where $\Delta\bar{\lambda} \ll 1$. Figure 2-7 shows the plot of the amplification gain against the characteristic radius $\Gamma = \frac{R}{r}$ for a maximum free displacement of a typical PZT stack (42 micrometers of free displacement and a body length of 40 millimeters), a cap profile radius,r, of 30 millimeters, and center distance, λ_0, of zero. A wide range of amplification gains can be obtained by tuning the radii ratio, Γ.

In order to prevent slippage, and thus prevent unnecessary losses, friction must be minimized at the contact surfaces. Furthermore, increasing the normal force at the contact joint increases the force necessary to cause slippage. Therefore, the ideal configuration is if, in statics, the contact force is normal to the contact face throughout the entire stroke of the actuator regardless of the output force of the PZT stack.

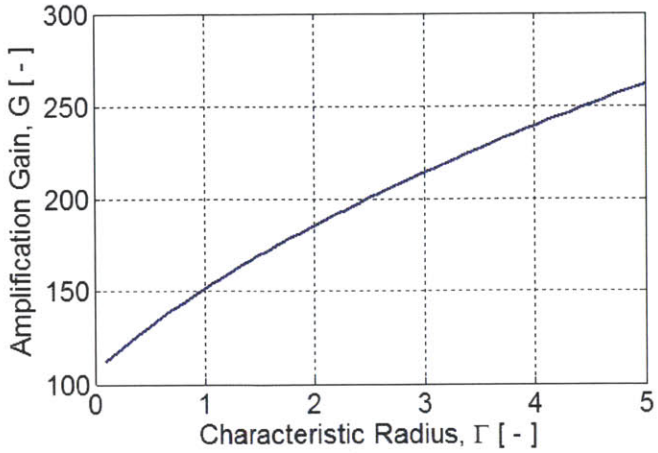

Figure 2-7: This plot relates the amplification gain of the buckling unit, G, to the characteristic radius, Γ, where $\Delta\lambda$ is held constant at 42 micrometers, the free displacement of the PZT stack. The center distance, λ_0, is zero and the cap profile radius, r, is 30 millimeters.

Provided that the caps and ground/keystone profiles are symmetric, this is accomplished by setting λ_0 to zero. If λ_0 equals zero, the two contact points are symmetric about the center point of the PZT stack-cap assembly, point C in Fig. 2-8. Therefore, in statics, the balanced forces must be equal, collinear, opposite in direction, and intersect at point C, so as not to impose a moment. If the cap surface at every point along the stroke is perpendicular to the contact force, the profile becomes an arc whose center is coincident with the center of the PZT stack. Most significantly, this is entirely independent of the specific ground/keystone profile. While this particular constraint is valid only in statics, this configuration also maximizes the normal force creating the largest allowable frictional force before slippage.

2.2.2 Output Stability

Although the rolling contact joint satisfies the amplification and efficiency functional requirements, it expands the function of the preload. Due to the fact that a contact force can only be used in compression, a preload force is necessary to maintain contact between the caps and the ground/keystone. Fortunately, the anchor points for the preload element, shown in Fig. 2-9, can be placed on the ground and keystone to

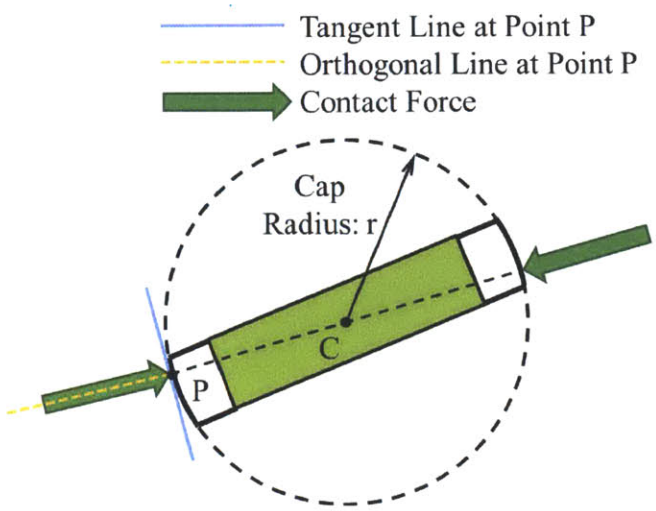

Figure 2-8: A force balance on the PZT-cap assembly accentuating the choice of radius r.

provide a preload to both the PZT stack and the contact surfaces.

The output is considered stable if the stiffness of the amplification mechanism is greater than zero when the output displacement and the input voltage are zero. There are two major parameters that affect the stability of the output: the magnitude of the preload force and the location of the anchor points. The magnitude of the preload force is ideally equal to that of the blocking force of the PZT stack as explained in a previous section. The anchor point position becomes a trade-off between stability versus the buckling unit's output displacement. Assuming the preload magnitude is equal to the PZT stack blocking force and continuing the assumption that the ground, keystone, and cap profiles are all circular, the "marginally stable" anchor point is at the center of the ground and keystone profile radii. The mechanism is considered marginally stable if the stiffness is zero, when the output displacement and the input voltage are zero. This geometric constraint would cause the preload angle, γ, shown in Fig. 2-9 to be equal to the ground contact angle, φ, throughout the entire stroke of the actuator. If the anchor points were moved inward, towards the contact point along the neutral axis, the output would become more stable but the stroke of the buckling amplification would become diminished. Conversely, if the anchor points were moved outward, away from the contact point along the neutral axis, the output

would start to become unstable with one stable point symmetrically on either side of the neutral axis, but would provide a larger maximum output displacement.

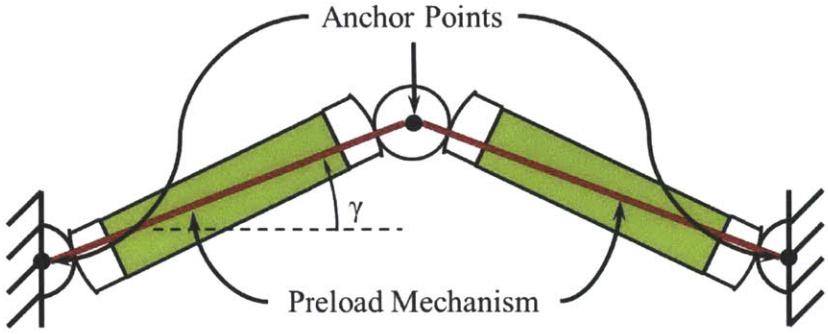

Figure 2-9: A schematic showing the location of the preload mechanism and its anchor points with respect to the keystone and ground.

Once the preload magnitude and anchoring points are established, a comprehensive model for the output displacement and force can be determined using a single generalized coordinate, the ground profile angle, φ, and the input voltage command, V_{PZT}. First, the force output of the PZT stack, modeled as a force source and spring in parallel, is as follows, where F_B is the blocking force, z_f is the free displacement, z_{PZT} is the absolute (meaning with reference to the initial position before preloading) PZT stack displacement, and V_{max} is the maximum allowed voltage.

$$F_{PZT}\left(z_{PZT}, V_{PZT}\right) = \frac{F_B}{z_f}\left(\frac{V_{PZT}}{V_{max}} z_f - z_{PZT}\right) \tag{2.11}$$

The PZT stack displacement, z_{PZT}, and the output displacement, y, can each be related to the generalized coordinate, φ, using geometry.

$$\begin{aligned} z_{PZT}\left(\varphi\right) &= \tfrac{2r(1+\Gamma)(1-\cos\varphi)}{\cos\{(1+\Gamma)\varphi\}} - z_f \\ y\left(\varphi\right) &= 2\left(R+r\right)\sin\varphi = 2r\left(1+\Gamma\right)\sin\varphi \end{aligned} \tag{2.12}$$

Equation 2.13 shows the explicit solution for the output force, where $F_{preload}$ is the preload force, equal in magnitude to the blocking force. Equation 2.14 classifies the

magnitude of the contact force, $|F_c|$, by equating the PZT stack force, F_{PZT}, to the z-directional component of the contact force, F_c.

$$F_b = (|F_c| - |F_{preload}|) \sin\varphi \tag{2.13}$$

$$|F_c| = \frac{F_{PZT}}{\cos\Gamma\varphi} \tag{2.14}$$

Combining Eqs. 2.11, 2.12, 2.13, and 2.14, yields Eq. 2.15, which describes the PZT stack force, F_{PZT}, and output force, F_b, as functions of only the system parameters, the state variable, φ, and the PZT voltage input, V_{PZT}.

$$\begin{aligned} F_{PZT}(\varphi, V_{PZT}) &= \tfrac{F_B}{z_f}\left(\left(\tfrac{V_{PZT}}{V_{\max}} + 1\right) z_f - \tfrac{2r(1+\Gamma)(1-\cos\varphi)}{\cos\{(1+\Gamma)\varphi\}}\right) \\ F_b(\varphi, V_{PZT}) &= (|F_c| - |F_{preload}|)\sin\varphi = \left(\tfrac{F_{PZT}(\varphi, V_{PZT})}{\cos(\Gamma\varphi)} - F_B\right)\sin\varphi \end{aligned} \tag{2.15}$$

2.2.3 Compliant Model

This comprehensive model, however, ignores significant losses associated with the compliance of the actual mechanism. As previously explained, a finite serial compliance and a non-zero parallel stiffness lessens the total cyclic work output. The major sources of serial and parallel compliance were identified as the contact stiffness at the rolling contact surface and the stiffness of the preloading element, respectively.

The stiffness of contacting surfaces is determined by the Hertzian contact stress. A higher force between the two surfaces produces more deformation, a larger contact area, and subsequently a greater stiffness. Applying this to the flexure-free, buckling mechanism where two rolling cylinders of the ground, keystone, and cap profiles are compressed, an estimate of stiffness can be obtained given by eq. 2.16. In the equation, the radii, R^*, elastic moduli, E, and Poisson's ratios, ν, are assumed to be equal for each surface. In addition, k_{joint} is the stiffness of the joint, w is the

width of cylinder, b is the contact length, δ is the relative displacement of the two cylinders, and P is the preload force. 2-10 plots the normalized stiffness of the joint as a function of the normalized preload force. The stiffness and force are normalized with respect to the PZT stack's stiffness and blocking force, respectively.

$$\begin{aligned} \frac{1}{E^*} &= \frac{2\left(1-\nu^2\right)}{E} \\ b &= \sqrt{\frac{8P}{\pi w R^* E^*}} \\ \delta &= \frac{P}{2wE^*}\left(\frac{2}{3} + 2\ln\frac{4R}{b}\right) \\ k_{joint} &= \left(\frac{\partial\delta}{\partial P}\right)^{-1} \end{aligned} \tag{2.16}$$

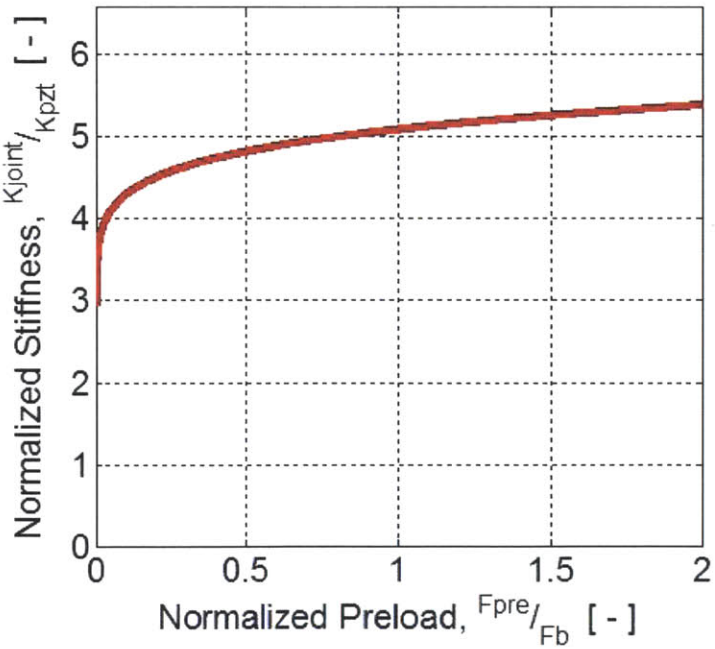

Figure 2-10: A plot showing the normalized joint stiffness as a function of the normalized preload. The stiffness and preload are normalized with respect to the PZT stack's stiffness and blocking force, respectively. The cap and ground material is steel and each profile radius is 30 millimeters.

Equation 2.15 is based on the assumption that the preload has a stiffness of zero and the rolling contact surface has an infinite stiffness. Equation 2.17 describes the magnitude of the adjusted preload force, $F_{preload}$, and the PZT stack displacement,

z_{PZT}, taking into account the modeled stiffnesses. In these equations, φ is the ground profile angle; F_B is the blocking force of the PZT stack; V_{PZT} is the input voltage to the PZT stack; r is the cap profile radius; Γ is the characteristic radius; k_{pre} is the stiffness of the preload element; and k_{joint} is the stiffness of the rolling contact joint and is approximated to be constant. The ideal and model results are shown in Fig. 2-11. The modeled cycle efficiency, defined as the ratio of the modeled work per cycle to the ideal work per cycle, is 70% for steel. This efficiency is robust to geometric changes, but is greatly affected by the material of the rolling contact.

$$\begin{aligned} |F_{preload}| &= F_B + k_{pre}\frac{1-\cos\varphi}{\cos\varphi}2r\,(1+\Gamma) \\ z_{PZT} &= \frac{2r(\Gamma+1)(1-\cos\varphi)k_{joint}\cos\Gamma\varphi}{(k_{joint}\cos\Gamma\varphi+2k_{PZT})\cos\{(1+\Gamma)\varphi\}} + \frac{2F_B V_{PZT}}{(k_{joint}\cos\Gamma\varphi+2k_{PZT})V_{\max}} \end{aligned} \tag{2.17}$$

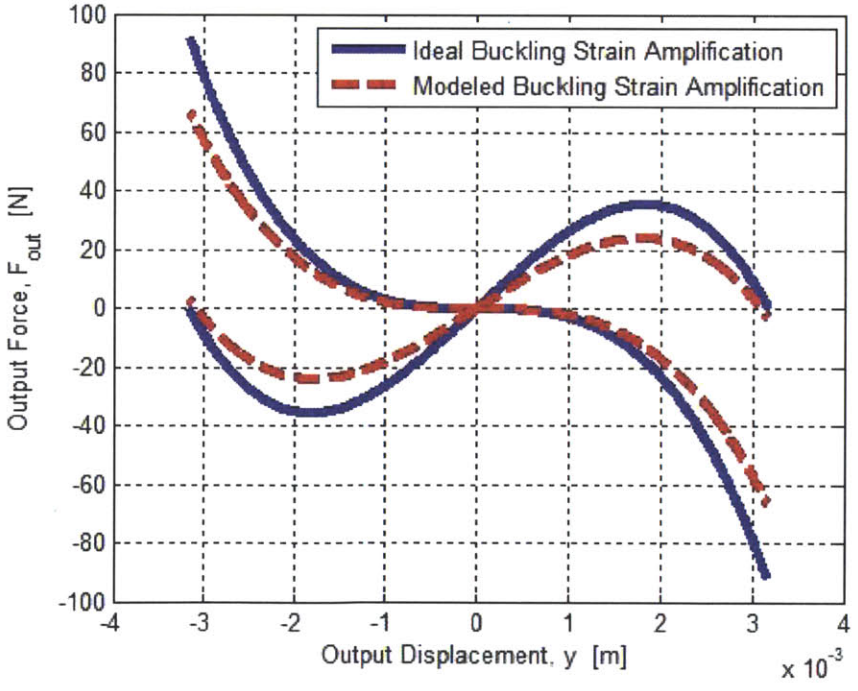

Figure 2-11: A plot of buckling force-displacement curve for both an ideal buckling displacement amplification mechanism (blue) and a modeled buckling displacement amplification mechanism (red). The system is based off of the AE1010D44H44F NEC-Tokin PZT, a characteristic radius, Γ, equal to one, and assumed to be made of carbon steel.

2.3 Actuator Redundancy

Due to the kinematic singularity at the neutral position, the direction that the amplification mechanism buckles is uncontrollable. Previous work dealt with this problem by adding an asymmetric stiffness to the rotation [17] or coupling a pair of buckling mechanisms such that they are out of phase [15] and then slightly staggering the charge timing. These methods, however, add to the parasitic stiffness and cost respectively. As mentioned previously, the output of the buckling mechanism is not meant to be interfaced with the load directly due to high degree of nonlinearity and the difficulty in precision control. Instead, several mechanisms are used in conjunction such that each mechanism is out of phase with all others; taking advantage of the redundancy two fold: to provide the necessary force to overcome the kinematic singularity, and to smooth the output force. Consider the simplified case in Fig. 2-12. There are several mechanisms all interfaced with a single gear-shaped cam. The magnitude of the slope of the profile, in this example, is considered to be constant with only the sign changing. If there was only one actuator, it would be uncontrollable at the singular point and the output force would vary dramatically. But as Fig. 2-13 demonstrates, the output force variation decreases as the number of actuators increases. Furthermore, this variation can be reduced further by smoothing the profile of the cam.

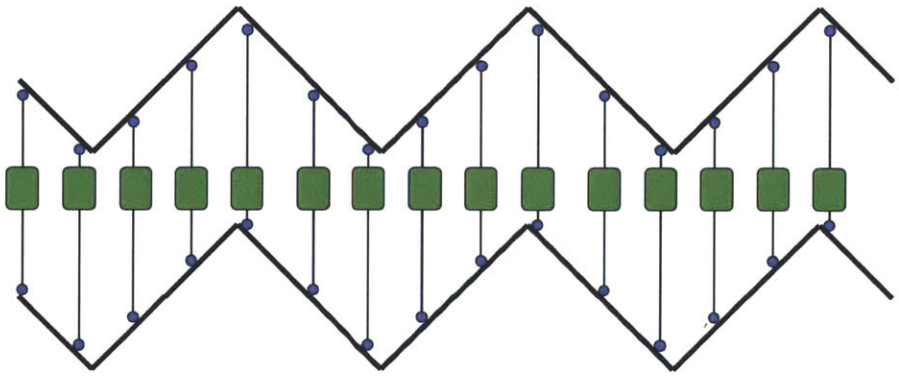

Figure 2-12: An example schematic of utilizing several out of phase amplification mechanisms to improve performance. Each green rectangle represents an independent buckling mechanism; the blue circles are the output interfaces; and the black track is the gear-shaped cam that translates horizontally.

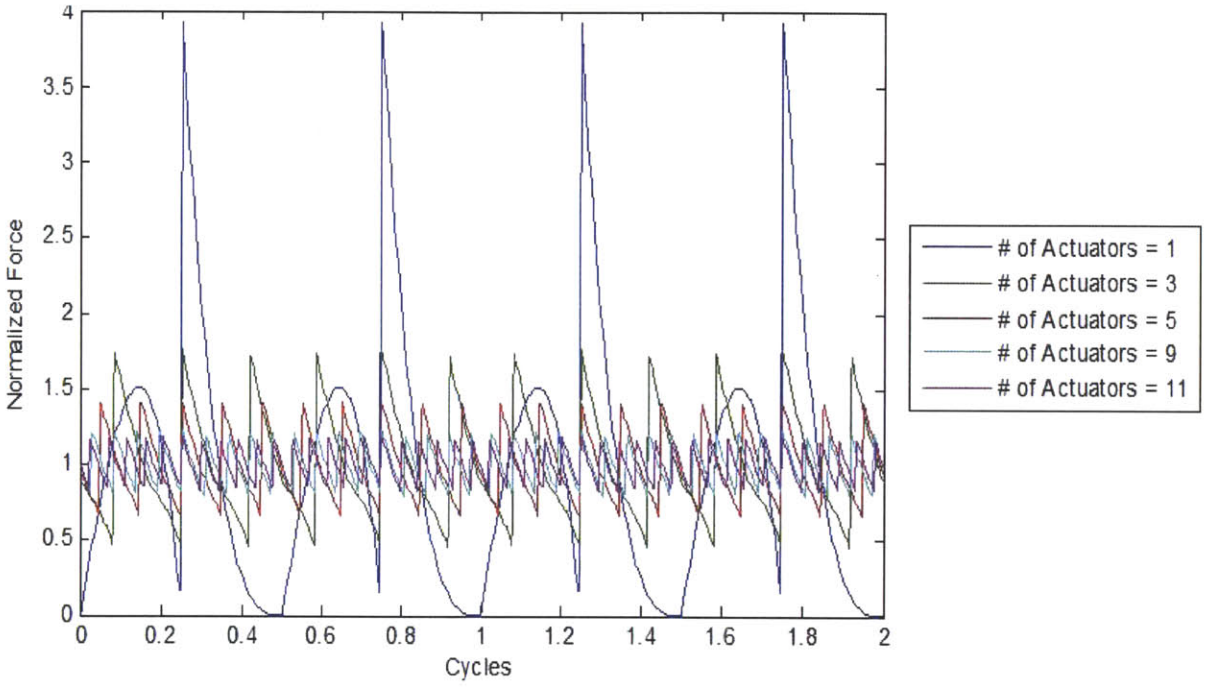

Figure 2-13: This plot shows the output force throughout two cam cycles highlighting the large variation for a small number of actuators.

Chapter 3

Mechanical Implementation

3.1 Preload and Restoring Force

3.1.1 Compliant Element

The previous chapter described a preload mechanism mounted in parallel to the PZT stack connecting the keystone and ground that is able to produce a preload force to improve both the PZT actuators' performance, by increasing the work output per cycle, and the rolling contact joint, by increasing the stiffness at the point of contact. Ideally, this would be a tensile force constant in magnitude regardless of the distance between the two points, which can be approximated when the stiffness of the PZT stack is much higher, at least two orders of magnitude, than that of the preload mechanism. Therefore, the stiffness element itself should be compliant so as not to degrade performance, but the size of the element should not dominate the size of the buckling unit. In order to minimize the size of the preload element, the stress within the material should be maximized. Therefore, as a lower bound estimate of the stiffness and area, Eqs. 3.1 and 3.2 respectively, assume the preload element is stressed to the yield strength of the material and provide a preload force equal to the blocking force of the PZT stack. Table 3.1 shows several possible materials and compares them to the stiffness and cross-sectional area of the PZT stacks using these equations, where F_{pre}, the preload force, is equal to the blocking force of the PZT

stack; L, the length of the stiffness mechanism is equal to PZT stack; and E and σ_y, are the elastic modulus and yield strength of the preload mechanism.

$$k_{pre} = \frac{EF_{pre}}{L\sigma_y} \tag{3.1}$$

$$A_{pre} = \frac{F_{pre}}{\sigma_y} \tag{3.2}$$

While rubber provides the best stiffness ratio, the large area ratio prevents it from being a viable solution. Both shape memory alloy (i.e. nitinol) and carbon fiber provide reasonable stiffness and area ratios.

Material	Stiffness Ratio	Area Ratio
Rubber - Nitrile	0.22	2450.
Carbon Fiber	2.93	1.54
Shape Memory Alloy - Nitinol	3.36	6.30
ABS Plastic	6.90	345.7
Aluminum - 6061-T6	14.98	25.12

Table 3.1: Stiffness and area ratios of possible compliant preload materials

3.1.2 Keystone Spring

The stabilization of the output/preload of the PZT stack can be simplified by recognizing that both $y \propto \sin\varphi$ and $F_b \propto \sin\varphi$, and therefore the preload mechanism can be replaced with a linear spring with respect to the output assuming a constant preload. The stiffness of the spring, k_y, is a function of the preload force, $F_{preload}$, characteristic radius, Γ, and cap radius, r, shown in Eq. 3.3.

$$k_y = \frac{F_{preload}}{2r\left(1+\Gamma\right)} \tag{3.3}$$

Mathematically, there is no difference between the two options, but physically this is a significantly easier and cheaper preload mechanism to implement. Furthermore, it allows for significantly more adjustment in the case of imperfections in alignment or preload. There are several assembly steps that must be addressed to achieve the desired preloading condition for the PZT stacks. First, consider that both ground profiles in Fig. 2-5 are initially unconstrained along the X-axis and the keystone is fixed. Placing the PZT-cap assemblies are placed in between the keystone and ground and the ground profiles are pushed inward towards the keystone until the reaction force on the ground profiles is equal to the desired preload force, $F_{preload}$. Then the ground profiles are fixed and the keystone is allowed to displace along the Y-axis. If the alignment is correct and the stiffness of the keystone spring, k_y, is tuned properly, the mechanism is "marginally stable" and the PZT stacks are preloaded.

3.2 Maintaining Alignment

3.2.1 Stack Alignment

A major functional requirement imposed by the rolling contact joint is the importance of the precise alignment of several components of the mechanism throughout its stroke utilizing only the preload mechanism and friction. Using the friction between two rolling surfaces to maintain the alignment can be unreliable, particularly in dynamic loading situations with vibrations. Introducing an angular misalignment, ξ, changes the relationship from the previous chapter to:

$$R\varphi = r\left(\theta - \xi\right) \Rightarrow \theta = \frac{R}{r}\varphi + \xi \tag{3.4}$$

Propagating the error through the equations yields the following correction to ??, note that the output displacement equation did not changed, but the maximum ground profile angle, φ_{max}, and subsequently the output displacement, is now asymmetric about the origin.

$$
\begin{aligned}
y &= 2r\left(1+\Gamma\right)\sin\varphi \\
F_{PZT}\left(\varphi, V_{PZT}, \xi\right) &= \frac{F_B}{z_f}\left(\left(\frac{V_{PZT}}{V_{\max}}+1\right)z_f - \frac{2r(1+\Gamma)(1-\cos\varphi)}{\cos\{(1+\Gamma)\varphi+\xi\}}\right) \\
F_b\left(\varphi, V_{PZT}, \xi\right) &= \left(|F_c| - |F_{preload}|\right)\sin\varphi = \left(\frac{F_{PZT}(\varphi, V_{PZT})}{\cos(\Gamma\varphi+\xi)} - F_B\right)\sin\varphi
\end{aligned}
\tag{3.5}
$$

Other mechanisms, such as gears, are not meant to take the large, radial loads that the joint experiences, but are able to maintain proper alignment. A hybrid design allows for alignment to be ensured within a desired tolerance while bearing the large forces through the large contact surface. Introducing a gear tooth and slot profile to the ground, keystone, and caps helps provide stability and maintains alignment. Figure 3-1 shows a realization of the hybrid rolling contact-gear tooth joint.

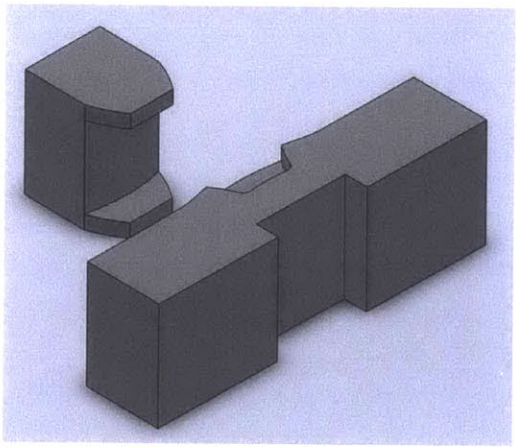

Figure 3-1: The gear tooth and slot disengaged in an isometric to show both the gear that maintains alignment, and the rolling surface that bears the large load.

The gear tooth and the mating slot are both shaped using an involute profile. An involute gear ensures the teeth remain in contact at all times. The meshing provides both a primary and secondary function. The primary function is to ensure that minimal slip exists between the cap and ground, and between the cap and the keystone. Utilizing a measured acceptable tolerance, initially the gear tooth would not be engaged with the slot at all; but if slipping started to occur, the gear tooth would engage the slot and limit the slipping to an acceptable upper bound. The performance of the buckling unit gracefully decays with misalignment, i.e. there

are no discontinuous changes to the force-displacement curve described in Eqs. 2.15 and 3.5; therefore, the acceptable amount of slop can be determined for a given application. The secondary function of the gear tooth and slot is to prevent the rotation of the PZT stack-cap assembly about the z-axis, where the z-axis is defined as the direction of the PZT stack displacement.

3.2.2 Keystone Alignment

An essential assumption made in the model presented is that the keystone must be constrained to a single degree of freedom, displacement in the Y-axis, as shown in Fig. 2-5. There are many possible ways to achieve this mechanical constraint, but in conjunction with the desired linear spring associated with the output for stability, a flexure based approach provides a solution to several functional requirements. Four flexures connected to the keystone, symmetric about the origin, i.e. the center of the keystone, would ensure reliably symmetric stiffness in all six degrees of freedom.

Due to the manufacturing process, however, flexures provide limited possibilities for adjustment. In particular, if the keystone is not aligned perfectly during the preloading process, the keystone will tend to drift once it is unconstrained. With typical compression linear springs this can be adjusted easily without sacrificing performance, but on their own, linear springs do not provide the other necessary constraints on the keystone. Therefore, a hybrid design is used because it is able to take advantage of both techniques.

Chapter 4

Kinematic Analysis and Control

4.1 Dynamics Model

4.1.1 Mass-Spring System Model

As mentioned previously the load connected to the amplification mechanism is a gear-shaped cam. For the purpose of the dynamics, however, the cam will be a sinusoidal track as depicted in Fig. 4-1. The gear has a mass, M, and a viscous damping coefficient, B. The gear track is a sinusoid with amplitude, A, and pitch, ω, such that the track displacement can be related to the output displacement of the buckling mechanism in Eq. 4.1. The amplitude of the track is guaranteed to be less than the maximum output displacement of the buckling mechanism to prevent overextension. Furthermore, the interaction between the buckling mechanism and the gear is modeled as frictionless and rigid.

$$y = A\sin(\omega X) \tag{4.1}$$

This output transmission also has a gain associated with it, G_2.

$$G_2 = \frac{dX}{dy} = \frac{1}{A\omega\sqrt{1-\left(\frac{y}{A}\right)^2}} \tag{4.2}$$

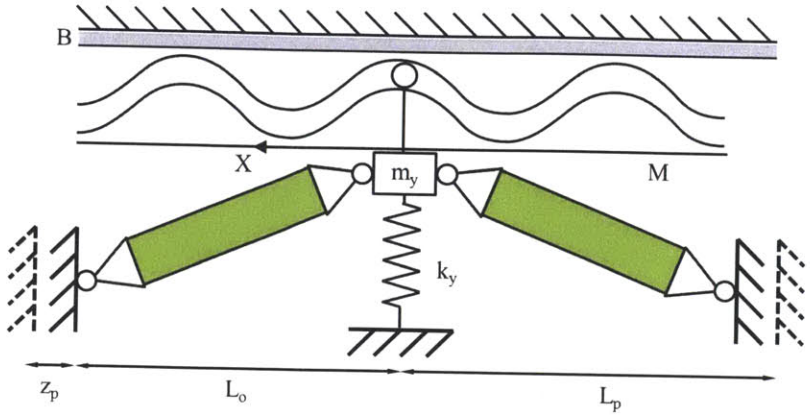

Figure 4-1: Schematic of the preloaded buckling mechanism connected to a geared output

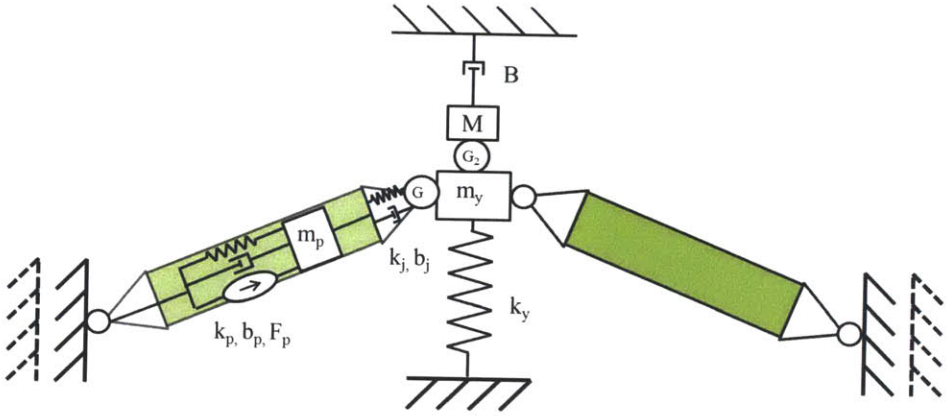

Figure 4-2: Schematic detailing the lumped parameters of the model

Figure 4-2 breaks down how the different components of the schematic are modeled. The PZT stack is modeled as a spring, damper, and force source in parallel connected to a mass. Ideally the rotational joints have an infinite radial stiffness, an infinite tangential compliance, and are lossless. However, in an actual system there are pertinent dynamics associated with the contact stiffness at these joints. The contact joint is modeled as a linear spring and damper connected in parallel. The keystone has a mass associated with it, which is connected to the grounded spring mentioned above. The load is a mass and damper connected in series. The stiffness associated with the coupling between the keystone and the gear is ignored. Finally, the force output of the force source, F_p, is related to the voltage across the PZT stack. The charging dynamics associated with this voltage add an order to the system making

the final model fifth order.

The system can then be described by the lumped parameter model in Fig. 4-3. Note that the system without charging dynamics is fourth order because there are two independent displacements, X and z, that are able to store kinetic and potential energy independently within the several masses and springs. Equation 4.1 describes the mechanism displacement, y, and Eq. 4.3 shows the displacement at the rotational joint, z_j, as a function of the generalized coordinates.

$$\begin{aligned} z_{total} &\approx \frac{y^2}{2L_o} = \frac{[A\sin(\omega X)]^2}{2L_o} = z_j + z \\ z_j &= \frac{[A\sin(\omega X)]^2}{2L_o} - z \end{aligned} \tag{4.3}$$

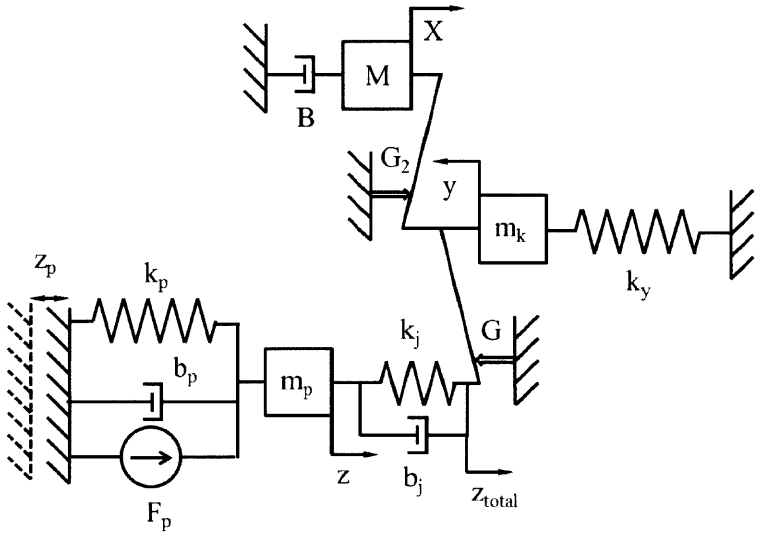

Figure 4-3: Lumped parameter model of the amplification mechanism and the output load.

4.1.2 Derivation of the Equations of Motion

The equations of motion can be simply derived using the Lagrange method. As mentioned previously, there are two independent displacements, X and z, that can be used as the generalized coordinates. The potential energy, V, kinetic energy, T, and their derivatives with respect to the generalized coordinates are shown in Eqs.

4.4 and 4.5, respectively.

$$\begin{aligned} V &= \tfrac{1}{2}k_p(z_p - z)^2 + \tfrac{1}{2}k_j {z_j}^2 + \tfrac{1}{2}k_y y^2 \\ \tfrac{\partial V}{\partial X} &= k_j z_j \tfrac{\partial z_j}{\partial X} + k_y y \tfrac{\partial y}{\partial X} \\ \tfrac{\partial V}{\partial z} &= -k_p(z_p - z) + k_j z_j \tfrac{\partial z_j}{\partial z} \end{aligned} \tag{4.4}$$

$$\begin{aligned} T &= \tfrac{1}{2}m_p \dot{z}^2 + \tfrac{1}{2}m_y \dot{y}^2 + \tfrac{1}{2}M\dot{X}^2 \\ \tfrac{\partial T}{\partial X} &= m_y \tfrac{\partial^2 y}{\partial X^2}\tfrac{\partial y}{\partial X}\dot{X}^2 \\ \tfrac{d}{dt}\left\{\tfrac{\partial T}{\partial \dot{X}}\right\} &= M\ddot{X} + m_y\left(2\tfrac{\partial^2 y}{\partial X^2}\tfrac{\partial y}{\partial X}\dot{X}^2 + \left(\tfrac{\partial y}{\partial X}\right)^2 \ddot{X}\right) \\ \tfrac{d}{dt}\left\{\tfrac{\partial T}{\partial \dot{z}}\right\} &= m_p \ddot{z} \end{aligned} \tag{4.5}$$

The non-conservative forces are associated with the dampers within the system and the piezoelectric force source. Thus the generalized forces of the system are:

$$\begin{aligned} \Xi_X &= -B\dot{X} - b_j \dot{z}_j \tfrac{\partial z_j}{\partial X} \\ \Xi_z &= -b_p \dot{z} - b_j \dot{z}_j \tfrac{\partial z_j}{\partial z} + F_p \end{aligned} \tag{4.6}$$

The equations of motion are therefore described by combining Eqs. 4.4, 4.5, and 4.6 using the Lagrange method.

$$\begin{aligned} \left[M + m_y\left(\tfrac{\partial y}{\partial X}\right)^2\right]\ddot{X} &= -m\tfrac{\partial^2 y}{\partial X^2}\dot{X}^2 - B\dot{X} - b_j \dot{z}_j \tfrac{\partial z_j}{\partial X} - k_j z_j \tfrac{\partial z_j}{\partial X} - k_y y \tfrac{\partial y}{\partial X} \\ m_p \ddot{z} &= -b_p \dot{z} - b_j \dot{z}_j \tfrac{\partial z_j}{\partial z} + F_p - k_j z_j \tfrac{\partial z_j}{\partial z} + k_p(z_p - z) \end{aligned} \tag{4.7}$$

Finally, the force source dynamics are associated with the RC circuit within the electrical domain, where τ is the electrical time constant and $F_{command}$ is the commanded force output. These electrical dynamics can be described by a low order approximation based on the electrical circuit described here [18].

$$\dot{F}_p = \frac{1}{\tau}\left(F_{command} - F_p\right) \tag{4.8}$$

4.2 Impedance Matching

Common design practice with DC motors is to match the expected load with the peak power output of the motor by properly specifying the motor and gearbox. Similarly with the buckling amplification mechanism, there exists an optimal frequency at which to run the actuator that will maximize the power output. Due to the significant nonlinearities within the system it is difficult to analytically predict the power transmission of the actuator and therefore, simulations were run using the dynamics described in Eqs. 4.7 and 4.8.

In addition to the dynamic equations, the control algorithm for the simulator is required. A simple binary controller is initially implemented, where switching is determined solely by the position of the keystone. The PZT stacks are charged when the keystone has no displacement and discharged at the maximum absolute displacement. Figure 4-4 shows the charging (red) and discharging (blue) explicitly.

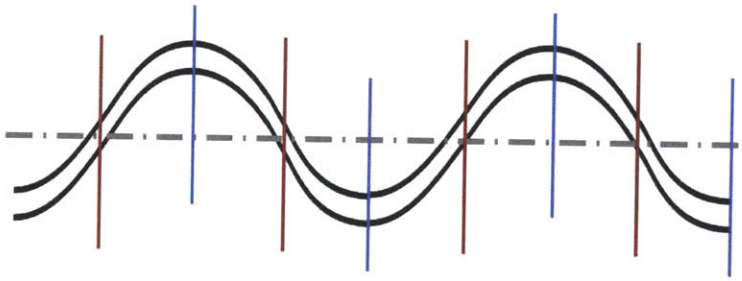

Figure 4-4: A schematic showing the initial control timing with respect to the gear track. Red is charging, blue is discharging.

The values of the parameters used in the simulation are shown in Table 4.1 and are based on a physical system to be used in future experiments to compare the results. The simulation was run while varying the gear damping, B. After the transient response subsides, the gear reaches a pseudo-steady state periodic velocity. It is not a true steady state velocity because there are minor fluctuations associated with the

oscillations of the buckling mechanism; however, from cycle to cycle the velocity does not change. At this point, the average power output from the buckling mechanism is equal to the average power dissipated in the gear damping. Therefore, the average power input from the PZT stack can be compared to the average power dissipated by the gear mechanism. Equations 4.9 and 4.10 detail the calculation of the average power input, $\bar{P}_{in}$, and output, $\bar{P}_{out}$, and the efficiency, η.

Parameter	Symbol	Value	Units
Length of PZT	L_p	50	mm
Mass of PZT	M_p	0.02	kg
Damping of PZT	b_p	2500	kg/s
Stiffness of PZT	k_p	1.19e5	N/mm
Damping of Joint	b_j	223	kg/s
Stiffness of Joint	k_j	4.76e5	N/mm
Mass of Keystone	m_y	0.262	kg
Stiffness of Keystone	k_y	100	N/mm
Mass of Gear	M	2	kg
Preload Length	z_p	42	μ s
Gear Amplitude	A	2	mm
Gear Pitch	ω	0.785	1/mm

Table 4.1: A list of the geometric and physical properties

$$\begin{aligned} \bar{P}_{out} &= mean\left\{B\dot{X}^2\right\} \\ \bar{P}_{in} &= mean\left\{F_p\dot{z}\right\} \end{aligned} \tag{4.9}$$

$$\eta = \frac{\bar{P}_{out}}{\bar{P}_{in}} \tag{4.10}$$

The maximum power and efficiency are limited predominantly by a phase lag between the output force and the output velocity. The source of the difference in phase can be attributed to the compliance of the joint and the charging of the PZT stack. Figures 4-5 and 4-6 show the average force and power output, and the efficiency, respectively, as functions of the gear velocity.

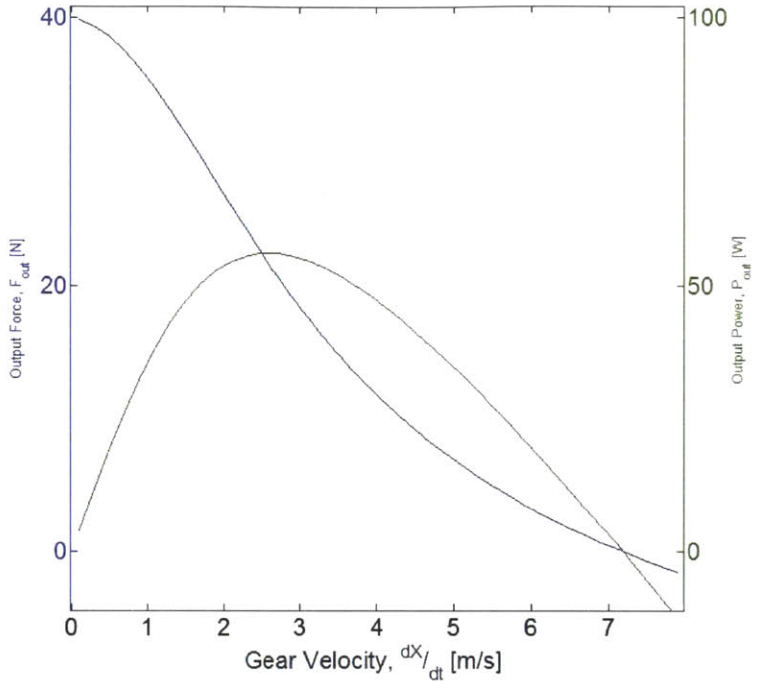

Figure 4-5: A plot showing the output force and power as a function of the gear velocity.

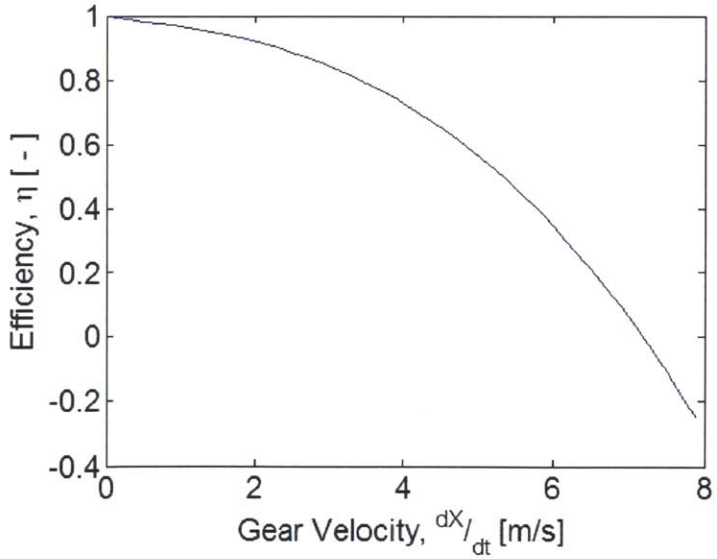

Figure 4-6: A plot showing the mechanical efficiency as a function of the gear velocity.

4.3 Control Timing

The buckling mechanism and slotted gear system is analogous to a combustion engine in several ways. First, the stroke has a fixed amplitude defined completely by kinematics and thus, the speed is directly related to the frequency of the piston/keystone. Second, the control is practically binary control and therefore dominated by the timing. The actuator transmits more power if the force and the velocity of the piston are in phase. Therefore, the initial timing control algorithm can be adapted by drawing insight from the automotive community, in particular, variable valve timing.

The phase lag associated with the joint compliance and the charging of the PZT stack can be compensated for by shifting the charging timing earlier by an amount, ΔX, shown in Fig. 4-7. This timing shift can be directly related to the gear velocity to increase the maximum output power and efficiency. Due to the complicated nonlinear dynamics and the pseudo-steady state velocity, this was determined solely through simulation. Figure 4-8 shows the power output for a variety of timing shifts. Figures 4-9 and 4-10 are presented to show the effects of variable vs. fixed timing on the system; power output and efficiency, respectively, are shown as functions of the gear velocity. The variable timing values depicted have been selected to produce the maximum power output. Using the data from the simulation, shown in Fig. 4-11, a fit was produced to anticipate the timing based solely on the measured pseudo-steady state velocity.

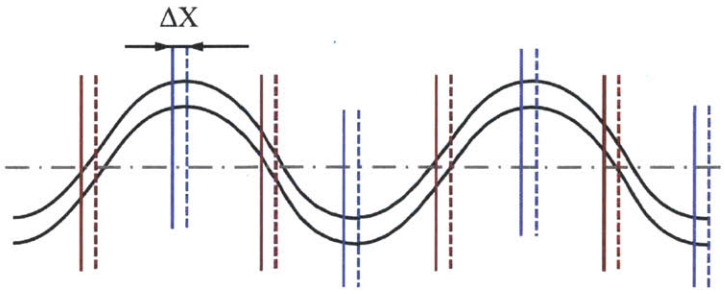

Figure 4-7: A schematic highlighting the timing shift assuming the gear is moving to the left.

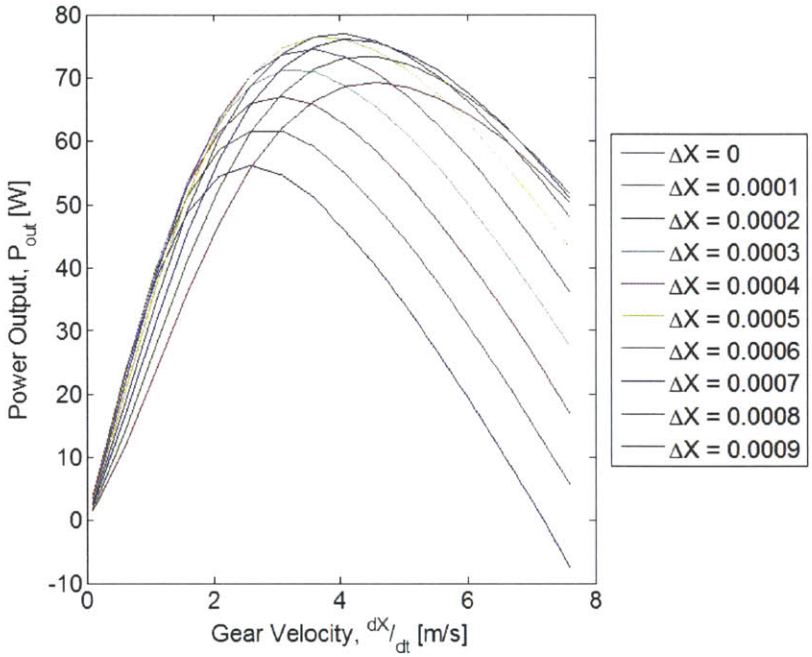

Figure 4-8: A plot comparing the output power for several timing shifts.

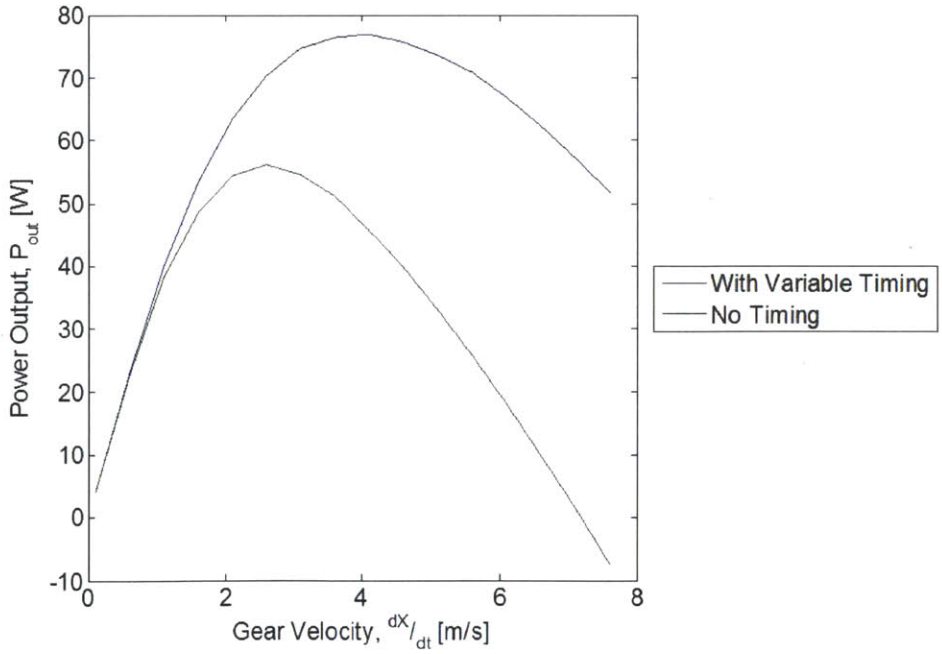

Figure 4-9: A plot comparing the output power for the standard and variable timing.

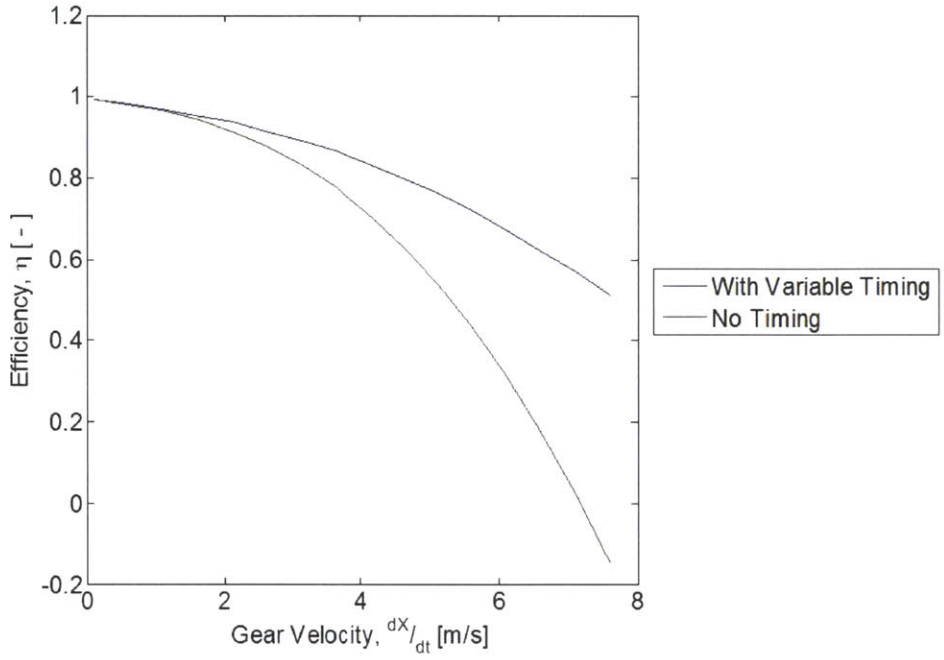

Figure 4-10: A plot comparing the efficiency for the standard and variable timing.

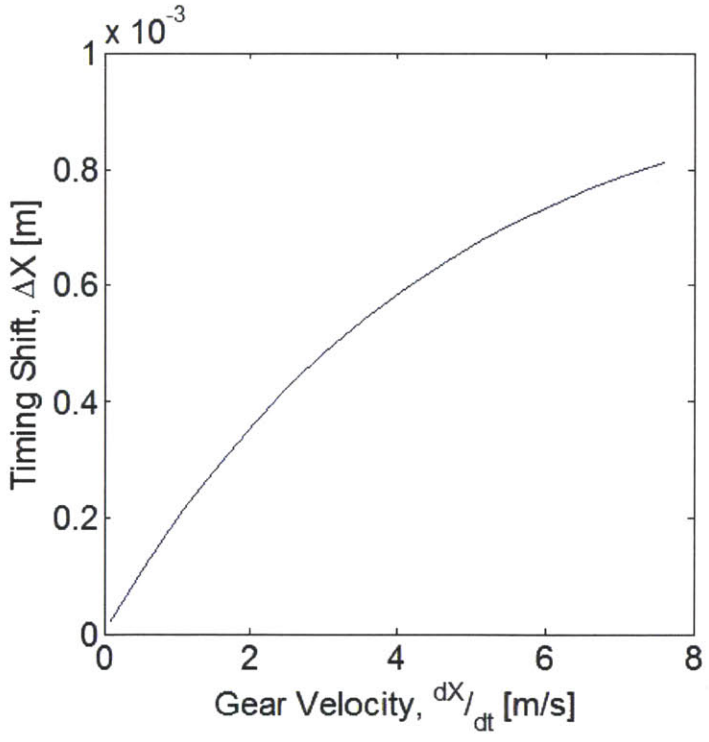

Figure 4-11: A plot showing the optimal timing shift as a function of the gear velocity.

Chapter 5

Results

A mechanical prototype was constructed to verify the static model and confirm the losses associated with the structural compliance. A labeled image of the buckling unit is shown in Fig. 5-1. The entire structure is made out of 4142 alloy steel. The two PZT stacks are PSt150hTc stacks from Piezomechanik, which have a blocking force of approximately 5000 Newtons and a free displacement of 42 micrometers. This particular design has a characteristic radius, Γ, equal to 1 and cap radius, r, of 30 millimeters. Shown on either side of the structure are the load cells that measure the preload force and the constraints that allow/prevent motion during the preloading process. Figure 5-2 provides a close up image of the PZT stack - Cap assembly including the three ABS plastic pieces used to provide alignment of the PZT stacks with respect to the caps.

Using the prototype, the force and displacement were measured simultaneously while the PZT stacks were both discharged and charged. These measurements were then compared to the expected results in Fig. 5-3. In this plot, the predicted lines are based off of Eqs. 2.12 and 2.15. These expected results take into account the compliance of the rolling contact joint and the frame. The maximum displacement in a single direction was 3.4 millimeters, which leads to a peak to peak displacement of 6.8 millimeters. Two major deviations are apparent. There is a significant deviation from the predicted while the PZT is discharged at large displacements. Also, both trials have a significant hysteresis. Possible sources of the hysteresis may be the

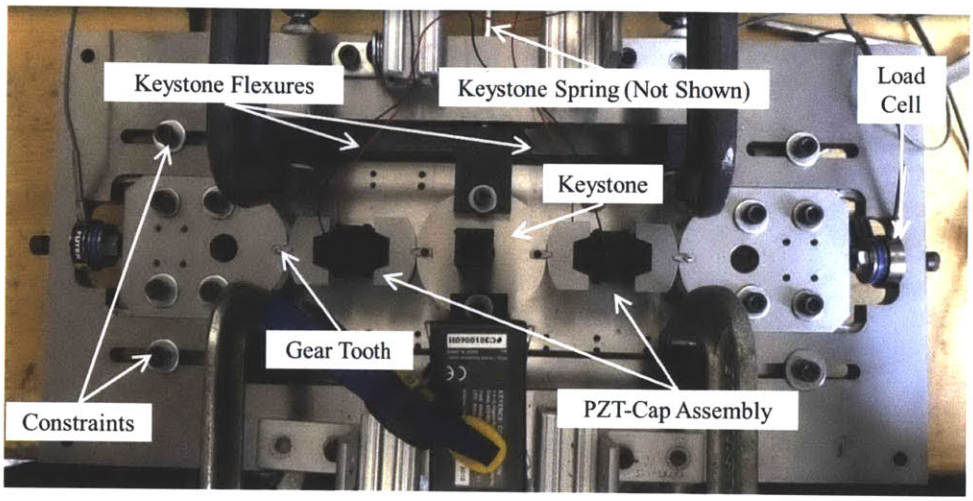

Figure 5-1: A labeled image of the assembled buckling unit.

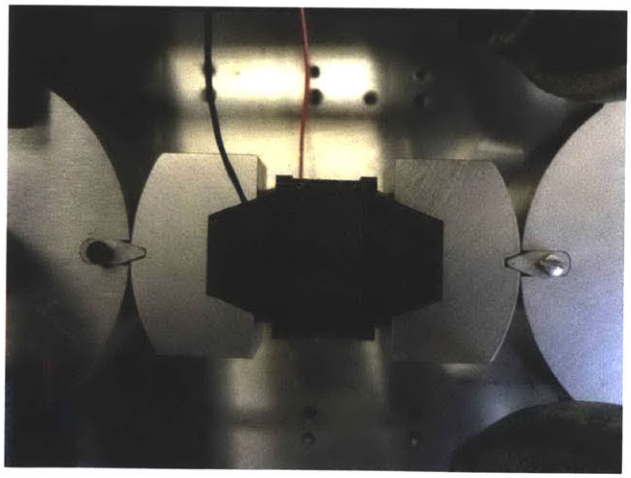

Figure 5-2: A close up image of the PZT stack - Cap Assembly.

rolling contact joint, in which case the hysteresis can be reduced with of the bearing surfaces, or the compression springs used to stabilize the keystone.

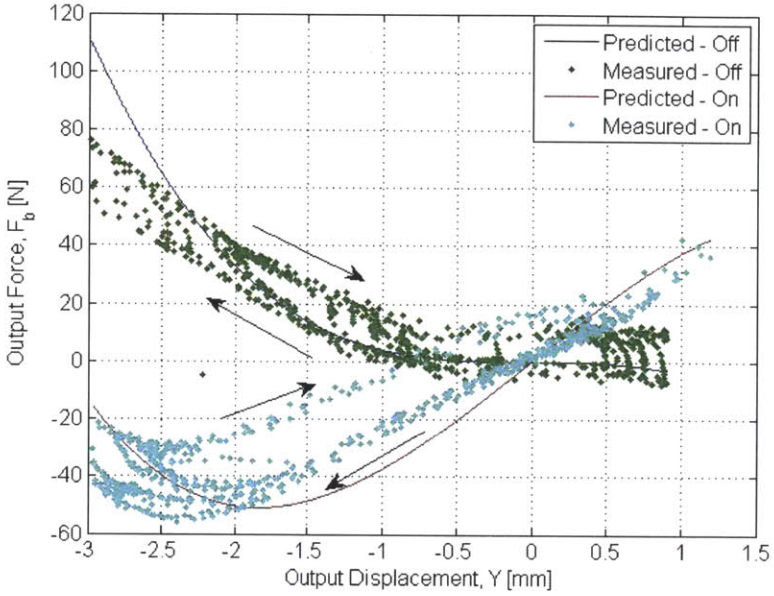

Figure 5-3: A plot comparing the predicted and measured force displacement. Note the arrows demonstrate the direction associated with the hysteresis.

Chapter 6

Conclusion

This thesis presented the design, analysis and implementation of a buckling displacement amplification mechanism that utilizes a rolling contact joint to reduce energy loss. The mechanism is able to amplify the displacement of PZT stack actuators two orders of magnitude in a single stage without sacrificing significant energy to the compliance of the mechanism. Furthermore, using the rolling contact joint allows for customizable amplification gains, while preventing any dependence on frictional forces to bear significant loads. Implementation details were discussed to preload the PZT stack so that the cyclic work output can be increased further, as well as, to maintain alignment and structural stability. A compliant model was created to predict what losses would occur to compare to a physical setup.

A dynamical analysis of the amplification mechanism under the assumption it interfaced with a linear gear cam with a mass-damper load. The dynamics were derived using a lumped parameter model of the mechanism. It was shown that there is an optimal speed that maximizes the power output for a given control timing. The characterized load can be matched to this optimal point by varying the pitch of the gear and thereby changing the gearing. By drawing upon the automotive industry's variable valve timing, an exploration into the possible benefits of adjusting the control timing is presented.

Finally, a physical prototype was created and tested. It was shown to produce peak to peak displacements of 6.8 millimeters, an amplification gain of over 150,

while still providing significant forces, over 50 Newtons. The output was shown to have a non-negligible hysteresis, which may be reduced by heat treatment of the manufactured bearing surfaces.

Bibliography

[1] J. Huber, N. Fleck, and F. Ashby, "The selection of mechanical actuators based on performance indices," *Mathematical, Physical and Engineering Sciences*, vol. 453, no. 1965, pp. 2185–2205, 1997.

[2] C. Yung, S. Or, H. Chan, P. Choy, and P. Liu, "Development of a piezoelectric induced-strain actuator with an innovative internal amplifying structure," in *Proceedings of the SPIE International Conference on Smart Materials and Structures*, pp. 22–33, May 2005.

[3] J. Juuti, K. Kordas, R. Lonnakko, V.-P. Moilanen, and S. Leppavouri, "Mechanically amplified large displacement piezoelectric actuators," *Sensors and Actuators A: Physical*, vol. 120, no. 1, pp. 225–231, 2005.

[4] C. Niezrecki, D. Brei, S. Balakrishnan, and A. Moskalik, "Piezoelectric actuation: State of the art," *The Shock and Vibration Digest*, vol. 33, no. 4, pp. 269–280, 2001.

[5] K. Choi, J. Lee, and S. Hata, "A piezo-driven compliant stage with double mechanical amplification mechanisms arranged in parallel," *Sensors and Actuators A: Physical*, vol. 161, no. 1, pp. 173–181, 2010.

[6] E. Furukawa, M. Mizuno, and T. Doi, "Development of a flexure-hinged translation mechanism driven by two piezoelectric stacks," *JSME International Journal*, vol. 38, no. 4, pp. 743–748, 1995.

[7] H. Ma, S. Yao, L. Wang, and Z. Zhong, "Analysis of the displacement amplification ratio of bridge-type flexure hinge," *Sensors and Actuators A: Physical*, vol. 132, no. 2, pp. 730–736, 2006.

[8] T. Secord and H. Asada, "A variable stiffness pzt actuator having tunable resonant frequencies," *IEEE Transactions on Robotics*, vol. 26, no. 6, pp. 993–1005, 2010.

[9] M. Muraoka and S. Sanada, "Displacement amplifier for piezoelectric actuator based on honeycomb link mechanism," *Sensors and Actuators A: Physical*, vol. 157, no. 1, pp. 84–90, 2010.

[10] J. Kim, S. Kim, and Y. Kwak, "Development and optimization of 3-d bridge-type hinge mechanisms," *Sensors and Actuators A: Physical*, vol. 116, no. 3, pp. 530–538, 2004.

[11] E. Ardelean, D. Cole, and R. Clark, "High performance 'v-stack' piezoelectric actuator," *Journal of Intelligent Material Systems and Structures*, vol. 15, no. 11, pp. 879–889, 2004.

[12] S. Hall, T. Tzianetopoulou, F. Straub, and H. Ngo, "Design and testing of a double x-frame piezoelectric actuator," in *Proceedings of the SPIE International Conference on Smart Materials and Structures*, pp. 26–37, March 2000.

[13] R. Fenn, J. Downer, D. Bushko, V. Gondhalekar, and N. Ham, "Terfenol-d driven flaps for helicopter vibration reduction," *Smart Materials and Structures*, vol. 5, no. 1, pp. 49–57, 1996.

[14] D. Neal and H. Asada, "Dynamic performance of nonlinear 100x displacement amplification piezoelectric actuator," in *Proceedings of the ASME 2010 Dynamics Systems and Control Conference*, pp. 65–72, September 2010.

[15] D. Neal and H. Asada, "Phased array piezoelectric actuators using a buckling mechanism having large displacement amplification and nonlinear stiffness," in *Proceedings of the IEEE International Conference on Robotics and Automation*, pp. 1661–1667, May 2010.

[16] D. Neal and H. Asada, "Design of cellular piezoelectric actuators with high blocking force and high strain," in *Proceedings of the ASME Dynamic Systems and Controls Conference*, pp. 779–786, October 2008.

[17] D. Neal and H. Asada, "Nonlinear, large-strain pzt actuators using controlled structural buckling," in *Proceedings of the IEEE International Conference on Robotics and Automation*, pp. 170–175, May 2009.

[18] P. Barragan, S. Tsukahara, and H. Asada, "Design of energy-saving pzt drive amplifiers for mobile and wearable physical assists," in *Proceedings of the ASME 2011 Dynamics Systems and Control Conference*, pp. 783–790, October 2011.